Hindawi
Geofluids
Volume 2022, Article ID 2837193, 10 pages
https://doi.org/10.1155/2022/2837193

Research Article

Micro- and Nanoscale Pore Structure Characterization and Mineral Composition Analysis of Clayey-Silt Hydrate Reservoir in South China Sea

Cheng Lu,[1,2,3] **Yuxuan Xia**,[3,4] **Xuwen Qin**,[1,2,5] **Chao Ma**,[1,2,5] **Hang Bian**,[6] **Donghui Xing**,[1,2,5] **and Hongfeng Lu**[1,2,5]

[1]*Guangzhou Marine Geological Survey, China Geological Survey, Guangzhou 511458, China*
[2]*National Engineering Research Center of Gas Hydrate Exploration and Development, Guangzhou, 511458 Guangdong, China*
[3]*Center of Oil & Natural Gas Resource Exploration, China Geological Survey, Beijing 100083, China*
[4]*State Key Laboratory of Petroleum Resources and Prospecting, China University of Petroleum, Beijing 102249, China*
[5]*Southern Marine Science and Engineering Guangdong Laboratory (Guangzhou), Guangzhou 511458, China*
[6]*School of Energy Resources, China University of Geosciences, Beijing 100083, China*

Correspondence should be addressed to Xuwen Qin; qinxuwen@163.com

Received 16 July 2022; Revised 14 August 2022; Accepted 22 September 2022; Published 17 November 2022

Academic Editor: Qingquan Liu

Natural gas hydrate is a kind of environmentally friendly unconventional energy with large reserves, which attract increasing attention in recent years. The microscopic pore structure and mineral composition of natural gas hydrate reservoir have a great influence on its seepage characteristics during exploitation. In this study, computed tomography and scanning electron microscope are used to obtain digital images of three clayey-silt natural gas hydrate reservoir samples in the Shenhu area of South China Sea, and then, the pore structure and the mineral composition of the samples are obtained after image processing. The result indicates that the clayey-silt samples show strong hydrophilic characteristics, small particles, good sorting properties, variable pore distribution, small average pore and throat radius, large porosity, and a large content of submicron pores. The mineral composition of the reservoir is mainly quartz and contains a certain amount of clay minerals, mainly illite, while the mineral composition of reservoir rich in microbial fossils is mainly carbonate. The results indicate that the pore structure and mineral composition of natural gas hydrate reservoirs in Shenhu area lay a foundation for the efficient development of the clayey-silt reservoir.

1. Introduction

Natural gas hydrate (NGH) is a kind of clean unconventional energy formed of water and natural gas under low temperature and high pressure [1, 2]. It is generally distributed in submarine sedimentary strata, land permafrost, and some deep-water lake sediments, with large reserves and shallow burial depth [3–6]. Many field production tests have been tried to exploit such resources from onshore and offshore natural gas hydrate deposits worldwide, including West Siberia [7], Alaska North Slope [8], Krishna-Godavari Basin [9], and Nankai Through [10]. In the Shenhu area of South China Sea, two production tests were carried out for gas hydrate reservoirs in 2017 and 2020 [11–13], respectively. During the development process, the gas production efficiency of the South China Sea hydrate reservoir fluctuates greatly, and the main controlling factors for the decline of the gas production efficiency in the later stage of development are still unclear. The reservoir samples and data obtained during the exploitation provided the basis for subsequent research on detailed seepage and development issues [11, 13–16]. Clarifying the complex mineral

composition and pore structure of reservoir sediments is one of the key scientific issues to improve the recovery efficiency of hydrate reservoirs [1, 9, 17].

The lithology of natural gas hydrate reservoirs in the Shenhu area is clayey silt with complex mineral composition. The overall mineral sources of the reservoir vary greatly and contain a certain amount of clay minerals [18, 19]. Meanwhile, the reservoir pore structure is complex, the sources of pores are diverse, and the size of pores also spans multiple scales. Effective characterization of pore structure is helpful to clarify the reservoir productivity [20]. Existing reservoir mineral and pore information is only obtained indirectly through geophysical logging, and there is a lack of direct characterization of gas hydrate reservoir sediments in the South China Sea using laboratory experiments. Digital rock technology, as a method of characterizing reservoir samples graphically, has been widely used in unconventional reservoirs such as shale gas and tight oil [21–24]. The scanning electron microscope (SEM) and microcomputed tomography (micro-CT) techniques are usually used to obtain high-resolution images for digital rock construction [25–27]. The mineral and pore structure features of in different rock samples can be visualized and quantified [28–31]. In terms of natural hydrate reservoirs, some works have also applied digital rock technology to study the hydrate synthesis-decomposition process [32–34], hydrate occurrence [35, 36], and seepage characteristics [37–40]. However, there is a lack of precise characterization of the mineral composition and micro- and nanoscale complex pore structure of gas hydrate reservoirs in the South China Sea by directly using high-precision imaging instruments, such as CT scanning and SEM imaging.

In this study, the micro-CT is used to obtain the three-dimensional grayscale images of the hydrate reservoir samples, and then, the pore and throat distribution are analyzed based on the processed binary image. Subsequently, two-dimensional nanoscale pore structure and mineral composition images are obtained by SEM, and the submicron pore characteristics and mineral composition of the sample are quantitatively analyzed.

2. Samples and Methods

The three NGH reservoir samples studied come from the Shenhu area. The location map and the strata of the reservoir are detailed in the study by [11, 39]. The lithology of the samples is mainly clayey silt with a median particle size of 12 μm [11]. The wettability angles are determined by sessile drop method which measures the angle between the bubble surface and the core surface using the KRÜSS DSA100E apparatus. As shown in Figure 1, the average wettability angles of three samples on both sides show strong hydrophilic characteristics (53.9°, 46.5°, and 48.3°).

2.1. Micro-CT. CT scans are performed on three NGH samples using a Zeiss MicroSCT-200micron CT scanner by iRock Technologies. The voltage and power used for scanning are 150 kV and 10 W, respectively. The pixel number and resolution are $2000 \times 2000 \times 1500$ and ~0.6 μm, respectively.

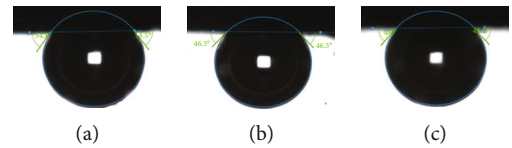

Figure 1: Measurement of wettability (a) sample 1, (b) sample 2, and (c) sample 3.

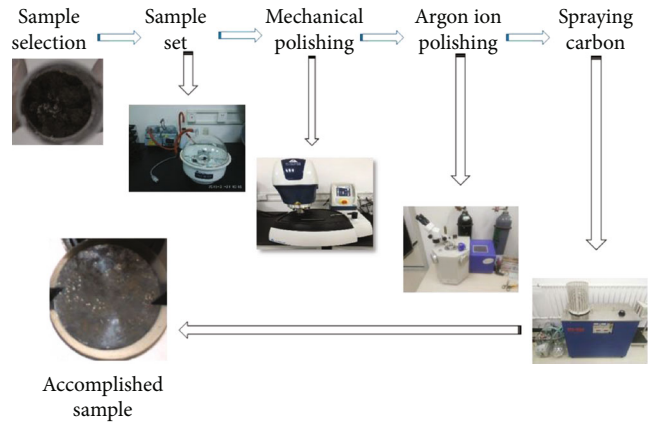

Figure 2: Electron microscope sample preparation flow chart of clayey-silt sample.

2.2. Preparation for Electron Microscope. Considering the lithology of the hydrate reservoir, dispersion happens when it contacts with water; meanwhile, the clay cementation and shrinkage will produce microcracks after drying. Therefore, targeted measures should be taken during the preparation of electron microscope samples to keep the drying temperature at 60°C to prevent the clay from losing water. During the glue injection process, using double injection is applied on both sides so that the epoxy resin can better fill the pores. The dry grinding method is used to polish samples to prevent particles from falling off after being exposed to water. The specific electron microscope sample preparation process is shown in the flow chart of Figure 2. The diameter of the accomplished round thin sample is 20 mm.

2.3. MAPS. Due to the limitation of the instrument itself, the resolution of the CT scan is up to the submicron level, resulting in the low accuracy in imaging nanolevel pores in the clay. Certain limitations in mineral identification also arise, viz., accurately identifying mineral types remain unattainable. Therefore, it is necessary to further supplement the two SEM methods, including modular automated processing system (MAPS) as well as the quantitative evaluation of minerals by scanning electron microscopy (QEMSCAN), to obtain the micro-nano pores and accurate mineral composition of hydrate reservoirs.

MAPS is aimed at samples requiring large-area observation (containing multiscale pore structures) [41]. A series of continuous and overlapping edges in a large number of

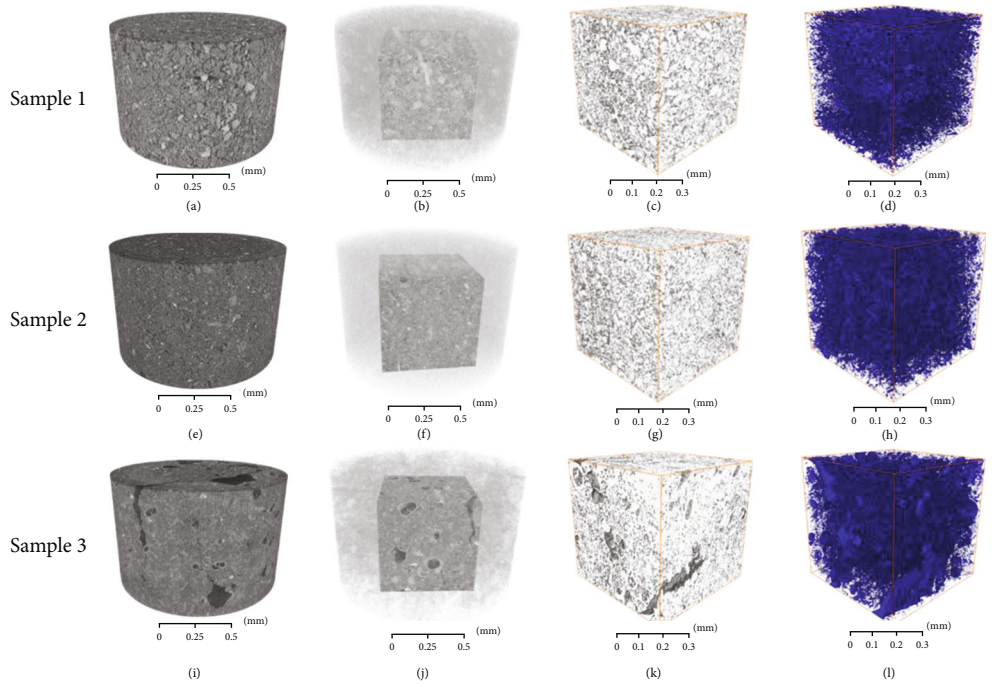

Figure 3: Original and processing CT image of three samples (a), (e), and (i) original CT grayscale image; (b), (f), and (j) the selected cube area for pore structure image in the original CT scan grayscale image; (c) (g), and (k) binarization pore image (gray is the pore); (d), (h), and (l) three-dimensional pore rendering image (blue is the pore).

high-resolution samples in a selected area is scanned. These small images will be stitched together to obtain a super high-resolution and large-area two-dimensional backscattered electron image. The MAPS image can be zoomed in or out arbitrarily like Google MAPS to observe multiscale rock characteristics. The test instrument used in this study is Helios NanoLab 650 of iRock Technologies.

2.4. QEMSCAN. QEMSCAN is a comprehensive automatic mineral detection method, which scans the surface of a sample with a high-energy electron beam accelerated along with a preset raster scan mode and produces a color map of the mineral assemblage's distribution characteristics [42]. The instrument emits an X-ray energy spectrum and provides information on the element content at each measurement point. Through the combination of backscattered electron grayscale image and X-ray intensity, the content of the element can be obtained and converted into a mineral phase. The test instrument used in this study is QEMSCAN 650F of iRock Technologies.

3. Results and Discussion

3.1. Micropore Structure Distribution. In this section, the microscale pore structures of samples are obtained by CT scan. Figure 3(a) shows the original CT scan grayscale image of sample 1, and small particles are visible with good sorting properties. The presence of large particles is rare, while it is rich in clay and debris. Most of the pores are developed in clay and microorganisms such as diatoms. Figures 3(b), 3(c), and 3(d) show the pore structure images obtained from the original gray image after post-processing (intercepting, filtering, and binarization) [43]. The corresponding CT porosity can also be extracted from the binarization pores (Table 1). It is more distinct that only a few connected macropores appeare in sample 1 from the binarization 3D image, yet most pores are isolated micropores. The CT porosity is 17.3%, and the connected porosity is 13.7%.

Table 1: CT porosity of three hydrate reservoir samples.

Sample	1	2	3
Porosity (%)	17.30	19.00	18.70
Connected porosity (%)	13.70	18.20	16.50
Average pore radius (μm)	1.29	1.15	3.04
Average throat radius (μm)	0.94	1.04	1.19

Based on pore structure space shown in Figure 3, Figure 4 shows pore and throat distribution curves obtained from nuclear magnetic resonance (NMR) and mercury injection simulation [44–47], respectively. The pore radius of sample 1 ranges from 0 μm to 12 μm, presenting a single-peak distribution with a maximum peak at 1 μm and an average pore radius of 1.29 μm (Table 1). The throat radius is in the range of 0~2.9 μm, and the distribution characteristic of the throat radius is multipeak. The maximum peak is located at 1.2 μm, and the average throat radius is 0.94 μm (Table 1).

Figure 3(e) shows the original CT grayscale image of sample 2. Compared with sample 1, sample 2 has the same small particles and good storability. Large particles are rarely distributed, while more amounts of clay and debris are presented. However, the pores are mostly elongated pores with

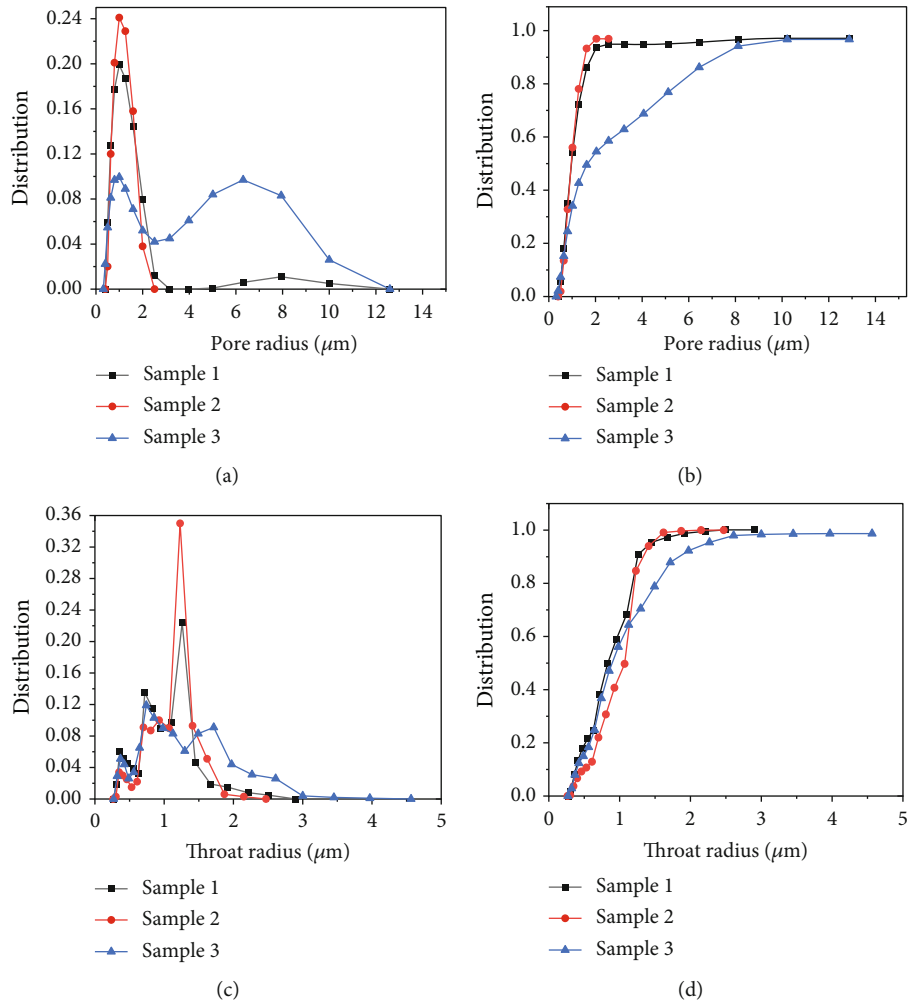

Figure 4: The comparison of microscale pore size distribution of three samples. (a) Pore radius distribution, (b) accumulation pore radius distribution, (c) throat radius distribution, and (d) accumulation throat radius distribution.

good pore connectivity and supplemented by macropores of microorganisms' origin. Figures 3(f), 3(g), and 3(h) show the pore structure image obtained from the original gray image after post-processing (intercepting, filtering, and binarization) [43] of sample 2. The binarization 3D image shows it is obvious that more large pores in sample 2 with better connectivity, and fewer isolated pores are observed. The CT porosity is 19.0% and the connected porosity is 18.2%.

The pore radius of sample 2 ranged from 0.4 μm to 2.5 μm, presenting a single-peak distribution with a maximum peak at 1.2 μm (Figure 4) and an average pore radius of 1.15 μm (Table 1). The throat radius is in the range of 0.3~2.5 μm, and the distribution characteristic of the throat radius is multipeak. The maximum peak is located at 1.2 μm, and the average throat radius is 1.04 μm (Table 1).

Figure 3(i) is the original CT grayscale image of sample 3. Compared with samples 1 and 2, sample 3 also shows better sorting with smaller particles while the rare occurrence of large particles. However, the pores mainly developed into fractures and round pores with good connectivity, and there are some microorganism-derived pores. Figures 3(j), 3(k), and 3(l) show the pore structure image obtained from the original gray image after post-processing (intercepting, filtering, and binarization) [43] of sample 3. It is even much clearer that the fractured macropores and circular macropores with good connectivity are in the majority in sample 3, from the binarization 3D image, while isolated pores still account for a certain part. The CT porosity is 18.7%, and the connected porosity is 16.5%.

The pore radius of sample 3 ranges from 0 μm to 12.5 μm, presenting a bimodal distribution corresponding to the bimodal pore radius values of 1 and 6.5 μm (Figure 4), respectively, and an average pore radius of 3.04 μm (Table 1). The throat radius is in the range of 0.3~19 μm, and the distribution characteristic of the throat radius is multipeak. The maximum peak is located at 0.8 μm, and the average throat radius is 1.19 μm (Table 1).

In summary, under the CT scan images of micron level, the pore and throat distributions of three samples are basic distribution within 19 μm, the average radius of pore and throat is between 1 and 3 μm, and porosities are in the range of 17~19%.Namely, although the overall pore size of the hydrate sample is small, a large number of pores still constitute a considerable pore space.

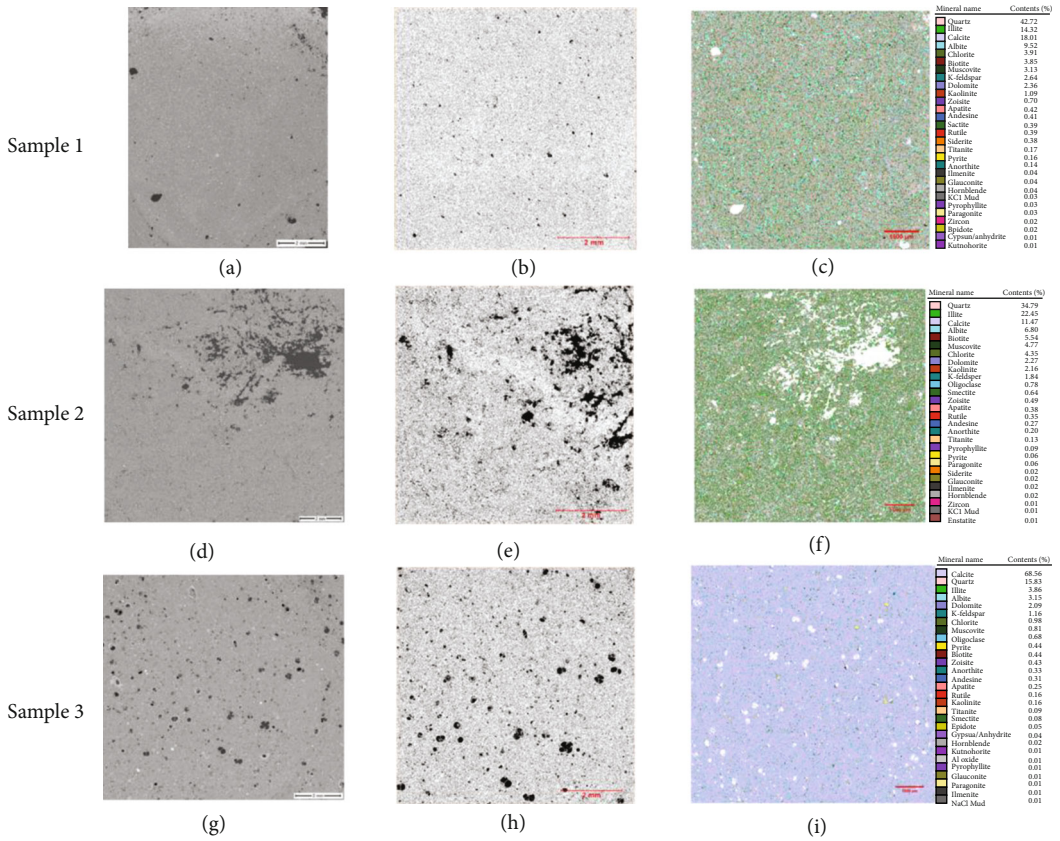

Figure 5: (a), (d), and (g) Grayscale image obtained by MAPS; (b), (e), and (h) binary pore segmentation image; and (c), (f), and (i) QEMSCAN imaging.

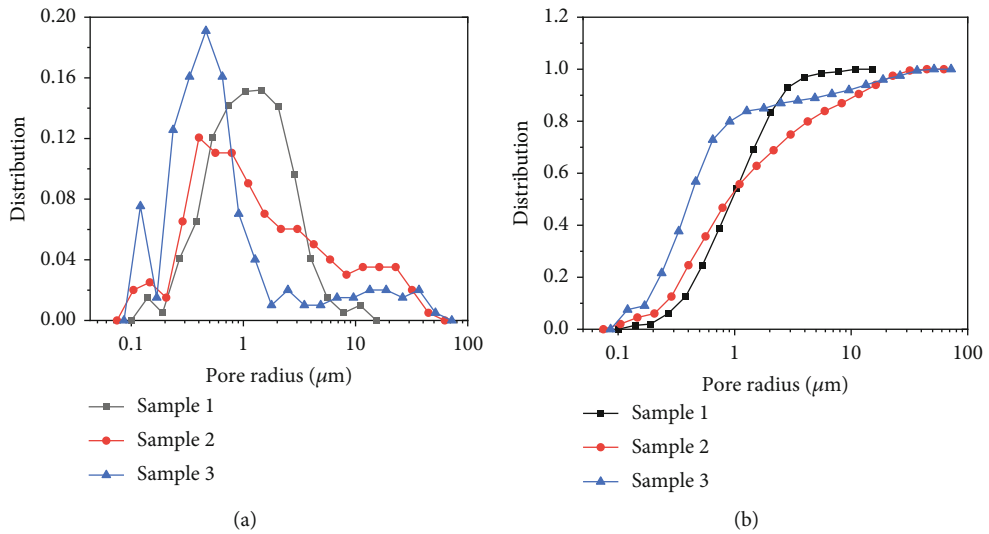

Figure 6: Comparison of (a) pore radius distribution and (b) accumulation pore radius distribution of three samples.

3.2. Micro- and Nanopore Structure Distribution. In this section, the micro-nano scale pore structures of samples are obtained by MAPS. Figure 5(a) is the electron microscope grayscale image of sample 1 obtained by MAPS after sample preparation. A total of 1,230 single scanning images are combined into an overall image, with a pixel number of 2048×1768 and a field of vision of 0.4×0.34 mm. The pixel number of the overall image is 56347×68053, and the field of view is 11.47×13.72 mm. The pixel resolution of the image is 195 nm.

To eliminate the large pores generated in the sample preparation process and improve the calculation efficiency,

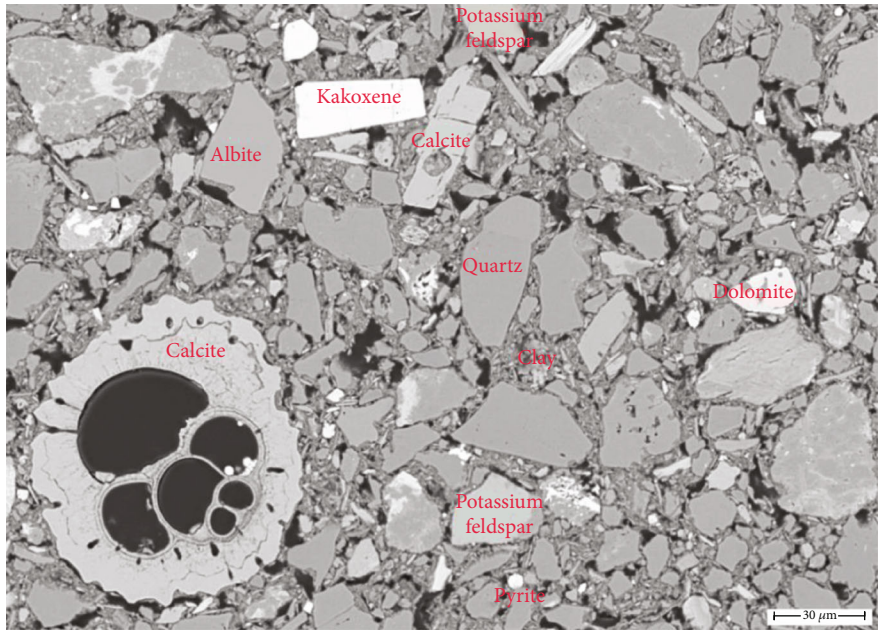

Figure 7: Typical mineral surfaces of reservoir samples.

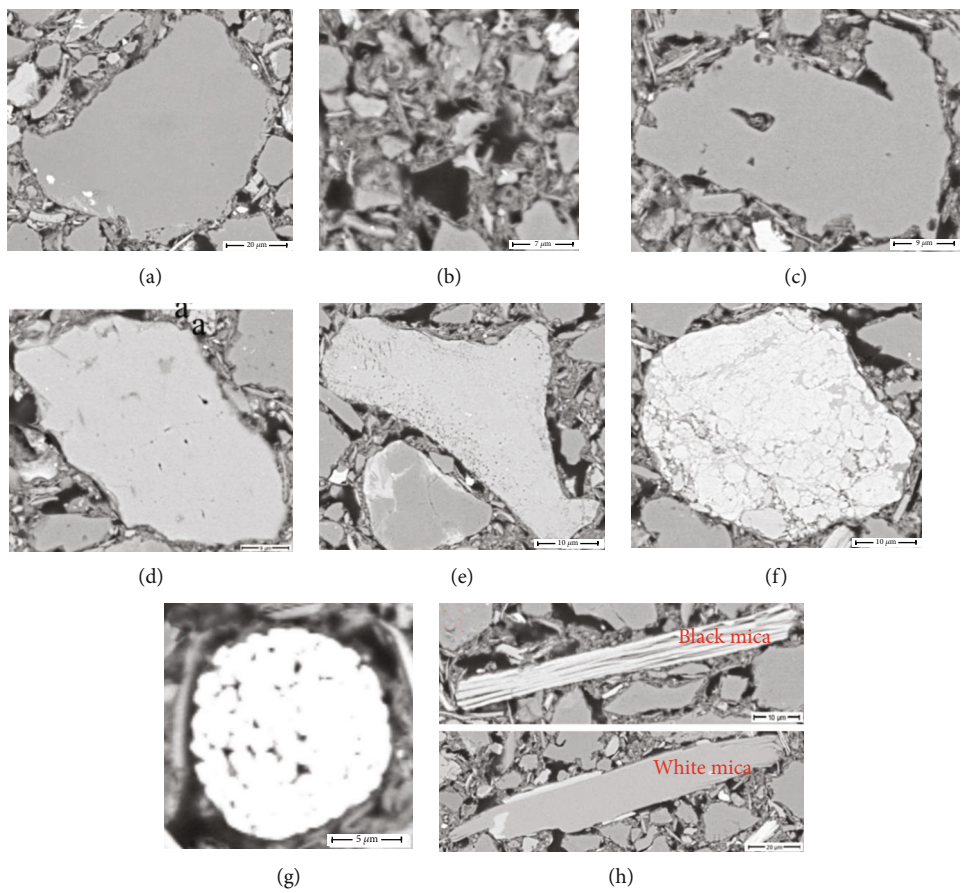

Figure 8: Different minerals: (a) quartz, (b) clay (mainly illite), (c) albite, (d) potassium feldspar, (e) calcite, (f) dolomite, (g) pyrite, and (h) mica.

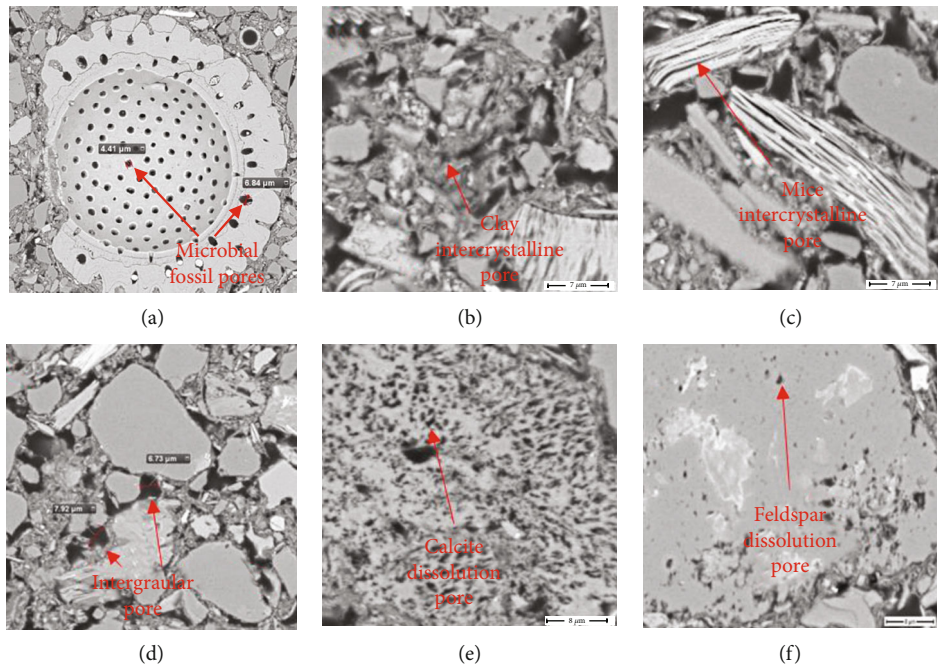

Figure 9: Different types of reservoirs pores: (a) microbial fossil pores, (b) clay intercrystalline pore, (c) mica intercrystalline pore, (d) intergranular pores, (e) calcite dissolution pore, and (f) feldspar dissolution pore.

the original grayscale image of sample 1 is first intercepted, and then, the binary segmentation is employed to divide the pores and the matrix, obtaining a segmented image of the binarized two-dimensional pore distribution of sample 1 (Figure 5(b)). The corresponding porosity can also be obtained from the binarized pore image, which is 16.78%. Figure 6 is the two-dimensional pore size distribution of sample 1 calculated from Figure 5(b). The simulation calculation results show that the sample pores have an average radius of 1.543 μm and a median radius of 1.341 μm, and the pores are distributed in a normal distribution.

Figure 5(d) is the electron microscope grayscale image of sample 2 obtained by MAPS after sample preparation. A total of 1,152 single scanning images are combined into an overall image, with a pixel number of 2048×1768 and a field of vision of 0.4×0.34 mm. The pixel number of the overall image is 59032×57733, and the field of view is 11.84×11.49 mm. The pixel resolution of the image is 195 nm.

To eliminate the large pores generated in the sample preparation process and improve the calculation efficiency, the original grayscale image of sample 2 is first intercepted, and then, the binary segmentation is employed to divide the pores and the matrix, obtaining a segmented image of the binarized two-dimensional pore distribution of sample 1 (Figure 5(e)). The corresponding porosity can also be obtained from the binarized pore image, which is 24.14%. Figure 6 is the two-dimensional pore size distribution of sample 2 calculated from Figure 5(e). The simulation calculation results show that the sample pores have an average radius of 4.1 μm and a median radius of 1.23 μm, and the pores are distributed in a normal distribution.

Figure 5(g) is the electron microscope grayscale image of sample 3 obtained by MAPS after sample preparation. A

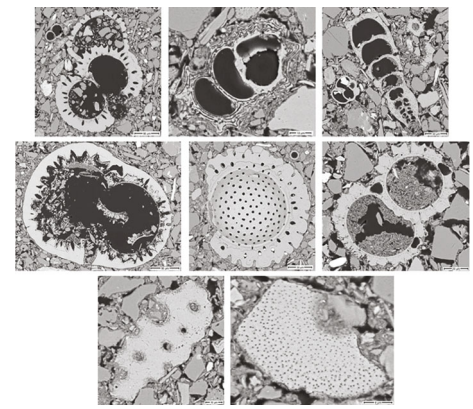

Figure 10: Reservoir fossils of different forms.

total of 1,023 single scanning images are combined into an overall image, with a pixel number of 2048×1768 and a field of vision of 0.4×0.34 mm. The pixel number of the overall image is 57204×52777 and the field of view is 11.47×10.54 mm. The pixel resolution of the image is 195 nm.

To eliminate the large pores generated in the sample preparation process and improve the calculation efficiency, the original grayscale image of sample 3 is first intercepted, and then, the binary segmentation is employed to divide the pores and the matrix, obtaining a segmented image of the binarized two-dimensional pore distribution of sample 1 (Figure 5(h)). The corresponding porosity can also be obtained from the binarized pore image, which is 20.77%. Figure 6 is the two-dimensional pore size distribution of sample 3 calculated from Figure 5(h). The simulation calculation results show that the sample pores have an average

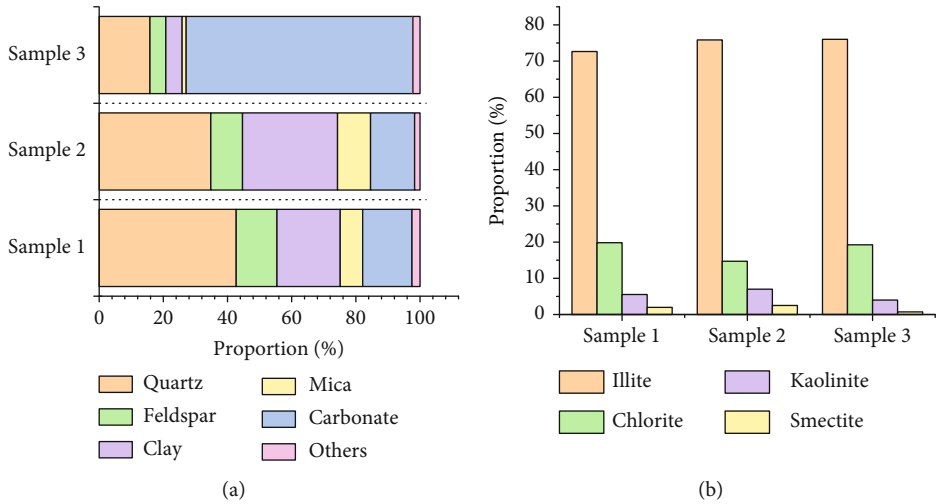

Figure 11: Comparison of (a) mineral and (b) clay contents of three samples.

radius of 2.86 μm and a median radius of 0.5 μm, and the pores are distributed in a normal distribution.

3.3. Mineral Composition. In this section, the mineral compositions of samples are obtained by QEMSCAN. Figure 5(c) shows the QEMSCAN result of sample 1, with a scan accuracy of 5 μm and a scan area of 11 × 11 mm. The mineral of sample 1 is mainly quartz, whose proportion is less than 50%; the proportion of feldspar is 12.16%; the proportion of carbonate is 15.37%; and the content of clay is close to 20%. Clay is mainly composed of illite (72.65%) and contains a certain amount of mica (6.98%).

Figure 5(f) shows the QEMSCAN result of sample 2, with a scan accuracy of 5 μm and a scan area of 11 × 11 mm. The mineral of sample 2 is mainly quartz, whose proportion is less than 35%, the proportion of feldspar is 9.89%, and the proportion of carbonate is 13.74%, and high in clay, which is close to 30%. Clay is mainly composed of illite (72.65%) and contains a certain amount of mica (6.98%).

Figure 5(i) shows the QEMSCAN result of sample 3, with a scan accuracy of 5 μm and a scan area of 11 × 11 mm. The mineral of sample 3 is mainly calcite, whose proportion is 69%; the proportion of quartz is less than 16%; and the proportion of feldspar is 5%, and low in clay, which is close to 5.1%. Clay is mainly composed of illite (76.02%).

3.4. Typical Minerals and Pores. Observing the MAPS images at different scales and comparing the mineral analysis results of the three samples, the particles of quartz and feldspar in the reservoir are relatively large and poor in roundness. The foraminifer fossils are mainly calcite. Clay particles are small and fill between quartz and feldspar, mainly illite (Figures 7 and 8).

Observing the MAPS images of three samples at different scales, the pore types of clayey-silt reservoirs can be divided into microbial fossil pore, intercrystalline pore, intergranular pore, and dissolution pore (Figure 9). Among them, clay pores and microbial fossil pores take up a relatively large proportion of the total pores. There are many microbial fossils in the hydrate reservoir, most of which are foraminifera, which can be used as a typical feature of the reservoir (Figure 10).

Table 2: Pore results of three samples obtained by MAPS.

Sample	1	2	3
Porosity (%)	16.78	24.14	20.77
Average pore radius (μm)	1.543	4.1	2.86
Median pore radius (μm)	1.341	1.23	0.6
Submicron pore fraction (%)	38.9	45	75

3.5. Comparison of Minerals and Pores. A comprehensive comparison of the mineral of the three samples shows that the mineral content and distribution of samples are quite different (Figure 11). Sample 1 has similar mineral properties to sample 2, with relatively high quartz content and a certain amount of clay. The minerals of sample 3 are mainly carbonate, which should be related to the fossil minerals.

From the comparison of the two-dimensional pore distributions of the three samples, the pore distributions of different samples are also quite different (Figure 6). Under the nanolevel SEM image, all three samples have a large number of submicron pores. Submicron pores of samples 1 and 2 account for 38.9% and 45%, respectively. As the reservoir minerals of sample 3 are mainly carbonate, there are many submicron pores, accounting for 75% (Table 2).

4. Conclusions

In this study, micro-CT and nano-SEM are applied to obtain digital images of clayey-silt hydrate reservoir samples in the South China Sea, and the pore structure characteristics and mineral compositions of the reservoir samples analyzed based on the images. The following conclusions can be derived:

(1) Hydrate samples show strong hydrophilic characteristics. Under the resolution of micro-CT, the clayey-

silt reservoir samples have small particles and good sorting properties and are rich in clay and debris contents. The pore morphology characteristics are variable, and the pore types are mainly clay and microorganisms' pores. The pore and throat radius are distributed below 19 μm, but the porosity is large, indicating that a large number of small pores constitute a relatively considerable pore space

(2) Under the resolution of SEM, the pore types of clayey-silt reservoirs can be divided into microbial fossil pore, intercrystalline pore, intergranular pore, and dissolution pore. Among them, clay pores and microbial fossil pores account for a relatively large proportion of the total pores. The pore distributions of different samples vary greatly, but they all have submicron pores with larger content

(3) There are obvious differences in the mineral compositions of the three clayey-silt samples. Samples 1 and 2 are mainly composed of quartz and contain a certain amount of clay, which is mainly illite. The mineral composition of sample 3 is mainly carbonate, which is speculated to be caused by fossil minerals

Data Availability

The data used to support the findings of this study are available from the corresponding author upon request.

Conflicts of Interest

The author(s) declare(s) that they have no conflicts of interest.

Acknowledgments

The authors are grateful to the National Natural Science Foundation of China (No. 51991365); the China Geological Survey Project (No. DD20211350); the Key Program of Marine Economy Development (Six Marine Industries) Special Foundation of Department of Natural Resources of Guangdong Province [2021]56; and the Guangdong Major Project of Basic and Applied Basic Research (No. 2020B0301030003).

References

[1] R. Shaibu, C. Sambo, B. Guo, and A. Dudun, "An assessment of methane gas production from natural gas hydrates: challenges, technology and market outlook," *Advances in Geo-Energy Research*, vol. 5, no. 3, pp. 318–332, 2021.

[2] E. D. Sloan Jr., "Fundamental principles and applications of natural gas hydrates," *Nature*, vol. 426, no. 6964, pp. 353–359, 2003.

[3] Y. Cui, C. Lu, M. Wu, Y. Peng, Y. Yao, and W. Luo, "Review of exploration and production technology of natural gas hydrate," *Advances in Geo-Energy Research*, vol. 2, no. 1, pp. 53–62, 2018.

[4] K. A. Kvenvolden, "Gas hydrates—geological perspective and global change," *Reviews of Geophysics*, vol. 31, no. 2, pp. 173–187, 1993.

[5] Y. F. Makogon, S. A. Holditch, and T. Y. Makogon, "Natural gas-hydrates—a potential energy source for the 21st century," *Journal of Petroleum Science and Engineering*, vol. 56, no. 1-3, pp. 14–31, 2007.

[6] H. Sun, B. Chen, W. Pang, Y. Song, and M. Yang, "Investigation on plugging prediction of multiphase flow in natural gas hydrate sediment with different field scales," *Fuel*, vol. 325, article 124936, 2022.

[7] Y. F. Makogon and R. Y. Omelchenko, "Commercial gas production from Messoyakha deposit in hydrate conditions," *Journal of Natural Gas Science and Engineering*, vol. 11, pp. 1–6, 2013.

[8] R. B. Hunter, T. S. Collett, R. Boswell et al., "Mount Elbert gas hydrate stratigraphic test well, Alaska north slope: overview of scientific and technical program," *Marine and Petroleum Geology*, vol. 28, no. 2, pp. 295–310, 2011.

[9] R. Boswell, J. Yoneda, and W. F. Waite, "India national gas hydrate program expedition 02 summary of scientific results: evaluation of natural gas-hydrate-bearing pressure cores," *Marine and Petroleum Geology*, vol. 108, pp. 143–153, 2019.

[10] K. Yamamoto, "Overview and introduction: pressure core-sampling and analyses in the 2012–2013 MH21 offshore test of gas production from methane hydrates in the eastern Nankai trough," *Marine and Petroleum Geology*, vol. 66, pp. 296–309, 2015.

[11] J.-F. Li, J.-L. Ye, X.-W. Qin et al., "The first offshore natural gas hydrate production test in South China Sea," *China Geology*, vol. 1, no. 1, pp. 5–16, 2018.

[12] X. W. Qin, C. Lu, P. K. Wang, and Q. Y. Liang, "Hydrate phase transition and seepage mechanism during natural gas hydrates production tests in the South China Sea: a review and prospect," *China Geology*, vol. 5, no. 2, pp. 201–217, 2022.

[13] J. L. Ye, X. W. Qin, W. W. Xie et al., "The second natural gas hydrate production test in the South China Sea," *China Geology*, vol. 3, no. 2, pp. 197–209, 2020.

[14] J. Cai, Y. Xia, S. Xu, and H. Tian, "Advances in multiphase seepage characteristics of natural gas hydrate sediments," *Chinese Journal of Theoretical and Applied Mechanics*, vol. 52, pp. 208–223, 2020.

[15] C. Dong, L. Wang, Y. Zhou et al., "Microcosmic retaining mechanism and behavior of screen media with highly argillaceous fine sand from natural gas hydrate reservoir," *Journal of Natural Gas Science and Engineering*, vol. 83, article 103618, 2020.

[16] Q. Liang, X. Xiao, J. Zhao et al., "Geochemistry and sources of hydrate-bound gas in the Shenhu area, northern South China Sea: insights from drilling and gas hydrate production tests," *Journal of Petroleum Science and Engineering*, vol. 208, article 109459, 2022.

[17] Z. R. Chong, S. H. B. Yang, P. Babu, P. Linga, and X.-S. Li, "Review of natural gas hydrates as an energy resource: prospects and challenges," *Applied Energy*, vol. 162, pp. 1633–1652, 2016.

[18] X. Wang, D. R. Hutchinson, S. Wu, S. Yang, and Y. Guo, "Elevated gas hydrate saturation within silt and silty clay sediments in the Shenhu area, South China Sea," *Journal of Geophysical Research: Solid Earth*, vol. 116, no. B5, article B05102, 2011.

[19] J. Ye, X. Qin, H. Qiu et al., "Data report: molecular and isotopic compositions of the extracted gas from china's first offshore natural gas hydrate production test in South China Sea," *Energies*, vol. 11, no. 10, p. 2793, 2018.

[20] B. Liu, R. Nakhaei-Kohani, L. Bai et al., "Integrating advanced soft computing techniques with experimental studies for pore structure analysis of Qingshankou shale in southern Songliao Basin, NE China," *International Journal of Coal Geology*, vol. 257, article 103998, 2022.

[21] M. Akbarabadi, S. Saraji, M. Piri, D. Georgi, and M. Delshad, "Nano-scale experimental investigation of in-situ wettability and spontaneous imbibition in ultra-tight reservoir rocks," *Advances in Water Resources*, vol. 107, pp. 160–179, 2017.

[22] M. J. Blunt, B. Bijeljic, H. Dong et al., "Pore-scale imaging and modelling," *Advances in Water Resources*, vol. 51, pp. 197–216, 2013.

[23] Y. Xia, J. Cai, E. Perfect, W. Wei, Q. Zhang, and Q. Meng, "Fractal dimension, lacunarity and succolarity analyses on CT images of reservoir rocks for permeability prediction," *Journal of Hydrology*, vol. 579, article 124198, 2019.

[24] C. Zou, D. Dong, S. Wang et al., "Geological characteristics and resource potential of shale gas in China," *Petroleum Exploration and Development*, vol. 37, no. 6, pp. 641–653, 2010.

[25] S. Kelly, H. El-Sobky, C. Torres-Verdín, and M. T. Balhoff, "Assessing the utility of FIB-SEM images for shale digital rock physics," *Advances in Water Resources*, vol. 95, pp. 302–316, 2016.

[26] Y. Li, X. Gao, S. Meng et al., "Diagenetic sequences of continuously deposited tight sandstones in various environments: a case study from upper Paleozoic sandstones in the Linxing area, eastern Ordos basin, China," *AAPG Bulletin*, vol. 103, no. 11, pp. 2757–2783, 2019.

[27] C. Madonna, B. S. Almqvist, and E. H. Saenger, "Digital rock physics: numerical prediction of pressure-dependent ultrasonic velocities using micro-CT imaging," *Geophysical Journal International*, vol. 189, no. 3, pp. 1475–1482, 2012.

[28] J. J. Kim, F. T. Ling, D. A. Plattenberger et al., "SMART mineral mapping: synchrotron-based machine learning approach for 2D characterization with coupled micro XRF-XRD," *Computers & Geosciences*, vol. 156, article 104898, 2021.

[29] J. J. Kim, F. T. Ling, D. A. Plattenberger, A. F. Clarens, and C. A. Peters, "Quantification of mineral reactivity using machine learning interpretation of micro-XRF data," *Applied Geochemistry*, vol. 136, article 105162, 2022.

[30] P. Lai, K. Moulton, and S. Krevor, "Pore-scale heterogeneity in the mineral distribution and reactive surface area of porous rocks," *Chemical Geology*, vol. 411, pp. 260–273, 2015.

[31] S. Tian, L. Bowen, B. Liu et al., "A method for automatic shale porosity quantification using an edge-threshold automatic processing (ETAP) technique," *Fuel*, vol. 304, article 121319, 2021.

[32] M. Holland and P. Schultheiss, "Comparison of methane mass balance and X-ray computed tomographic methods for calculation of gas hydrate content of pressure cores," *Marine and Petroleum Geology*, vol. 58, pp. 168–177, 2014.

[33] L. Lei, Y. Seol, J.-H. Choi, and T. J. Kneafsey, "Pore habit of methane hydrate and its evolution in sediment matrix—laboratory visualization with phase-contrast micro-CT," *Marine and Petroleum Geology*, vol. 104, pp. 451–467, 2019.

[34] D. Wang, Y. Li, C. Liu et al., "Study of hydrate occupancy, morphology and microstructure evolution with hydrate dissociation in sediment matrices using X-ray micro-CT," *Marine and Petroleum Geology*, vol. 113, article 104138, 2020.

[35] X. Chen, R. Verma, D. N. Espinoza, and M. Prodanović, "Pore-scale determination of gas relative permeability in hydrate-bearing sediments using X-ray computed micro-tomography and lattice Boltzmann method," *Water Resources Research*, vol. 54, no. 1, pp. 600–608, 2018.

[36] P. Wu, Y. Li, L. Wang et al., "Hydrate-bearing sediment of the South China Sea: microstructure and mechanical characteristics," *Engineering Geology*, vol. 307, article 106782, 2022.

[37] J. Cai, Y. Xia, C. Lu, H. Bian, and S. Zou, "Creeping microstructure and fractal permeability model of natural gas hydrate reservoir," *Marine and Petroleum Geology*, vol. 115, article 104282, 2020.

[38] Y. Konno, Y. Jin, T. Uchiumi, and J. Nagao, "Multiple-pressure-tapped core holder combined with X-ray computed tomography scanning for gas–water permeability measurements of methane-hydrate-bearing sediments," *Review of Scientific Instruments*, vol. 84, no. 6, article 064501, 2013.

[39] C. Lu, Y. Xia, X. Sun et al., "Permeability evolution at various pressure gradients in natural gas hydrate reservoir at the Shenhu area in the South China Sea," *Energies*, vol. 12, no. 19, p. 3688, 2019.

[40] P. Wu, Y. Li, X. Sun, W. Liu, and Y. Song, "Pore-scale 3D morphological modeling and physical characterization of hydrate-bearing sediment based on computed tomography," *Journal of Geophysical Research: Solid Earth*, vol. 125, no. 12, article e2020JB020570, 2020.

[41] Y. Li, J. Yang, Z. Pan, and W. Tong, "Nanoscale pore structure and mechanical property analysis of coal: an insight combining AFM and SEM images," *Fuel*, vol. 260, article 116352, 2020.

[42] Y. Li, J.-Q. Chen, J.-H. Yang, J.-S. Liu, and W.-S. Tong, "Determination of shale macroscale modulus based on microscale measurement: a case study concerning multiscale mechanical characteristics," *Petroleum Science*, vol. 19, no. 3, pp. 1262–1275, 2022.

[43] H. Dong and M. J. Blunt, "Pore-network extraction from micro-computerized-tomography images," *Physical Review E*, vol. 80, no. 3, article 036307, 2009.

[44] M. Z. Kalam, "Digital rock physics for fast and accurate special core analysis in carbonates," in *New Technologies in the Oil and Gas Industry*, 2012.

[45] O. Talabi, S. AlSayari, S. Iglauer, and M. J. Blunt, "Pore-scale simulation of NMR response," *Journal of Petroleum Science and Engineering*, vol. 67, no. 3-4, pp. 168–178, 2009.

[46] E. Toumelin, C. Torres-Verdín, and S. Chen, "Modeling of multiple echo-time NMR measurements for complex pore geometries and multiphase saturations," *SPE Reservoir Evaluation & Engineering*, vol. 6, no. 4, pp. 234–243, 2003.

[47] E. Toumelin, C. Torres-Verdín, B. Sun, and K.-J. Dunn, "Random-walk technique for simulating NMR measurements and 2D NMR maps of porous media with relaxing and permeable boundaries," *Journal of Magnetic Resonance*, vol. 188, no. 1, pp. 83–96, 2007.